Journal of Materials Chemistry C

ROYAL SOCIETY OF CHEMISTRY

PAPER

View Article Online
View Journal | View Issue

Cite this: J. Mater. Chem. C, 2021, 9, 3204

Implications of acceptor doping in the polarization and electrocaloric response of $0.9Pb(Mg_{1/3}Nb_{2/3})O_3–0.1PbTiO_3$ relaxor ferroelectric ceramics†

Andraž Bradeško,[a] Marko Vrabelj,[a] Lovro Fulanović,[a] Šarūnas Svirskas,[b] Maksim Ivanov,[b] Ringaile Katiliūte,[b] Džiugas Jablonskas,[b] Mantas Šimėnas,[b] Gediminas Usevičius,[b] Barbara Malič,[ac] Juras Banys[b] and Tadej Rojac*[ac]

In ferroelectrics, the effects of acceptor doping on electrical and electromechanical properties, often referred to as the "hardening" effects, are commonly related to domain-wall pinning mechanisms mediated by acceptor-oxygen-vacancy defect complexes. In contrast, the hardening effects in relaxor ferroelectric materials are complicated by the nano-polar nature of these materials, the associated dynamics of the polar nano-regions and their contribution to polarization, and the characteristic freezing transition between the ergodic and the non-ergodic phases. To shed light on this issue, in this study, we investigate the role of the acceptor (Mn) doping on the temperature-dependent broadband dielectric permittivity, high-field polarization–electric-field (*P*–*E*) hysteresis and electrocaloric (EC) response of $0.9Pb(Mg_{1/3}Nb_{2/3})O_3–0.1PbTiO_3$ (PMN-10PT) relaxor ferroelectric ceramics. The results suggest strong pinning effects, mediated by the acceptor–oxygen-vacancy defect complexes, which manifest similarly both in the ergodic and in the non-ergodic phases of PMN-10PT as revealed by the doping-induced suppression of the frequency dispersion of the permittivity maximum and pinched high-field hysteresis loops. In addition to these pinning effects, the Mn doping reduces the freezing temperature (T_f) by ~50 °C with respect to the undoped PMN-10PT. This is reflected in the EC response, which becomes less temperature dependent, making defect engineering a valuable approach for designing EC materials with an extended operational temperature range.

Received 14th December 2020,
Accepted 16th January 2021

DOI: 10.1039/d0tc05854h

rsc.li/materials-c

Introduction

In ferroelectrics, aliovalent (acceptor and donor) doping leads to the so-called "hardening" and "softening" effects, respectively, well known in $Pb(Zr,Ti)O_3$ (PZT) as one of the technologically most important methods for tailoring the electrical and electromechanical responses of this class of materials.[1–3] It is commonly accepted that hardening by acceptor doping, *e.g.*, in PZT and $BaTiO_3$, arises due to the presence of defect complexes of the acceptor-oxygen-vacancy type, which provide electric and elastic pinning effects to ferroelectric/ferroelastic domain walls.[4–7] Macroscopically, this pinning is reflected in pinched polarization–electric-field (*P*–*E*) hysteresis loops, increased coercive field, lowered dielectric and piezoelectric coefficients, and reduced losses.[1,2]

In contrast to "normal" ferroelectrics, exhibiting no relaxor behavior, the hardening effects by acceptor doping in relaxor ferroelectrics, such as $Pb(Mg_{1/3}Nb_{2/3})O_3–PbTiO_3$ (PMN-PT), are far less understood due to complications arising from the nano-polar nature of these materials and the associated relaxor behaviour characterized by the dispersive dielectric permittivity and the ergodic-to-non-ergodic transition at the freezing temperature (T_f).[8–11] For example, it is expected that the defect complexes will behave differently in the ergodic and non-ergodic states of PMN-PT due to the different range (short or long) of the polar order and the associated dynamics of the polar nanoregions or domain walls in these different polar states. In addition, although common aging effects have been confirmed in various acceptor-doped PMN-PT materials,[12] acceptor doping using Fe ions, for example, is not as efficient in hardening the properties as it is in non-relaxor PZT.[10] Further complications arise from the B-site chemical ordering in PMN-PT and similar relaxor ferroelectric materials as this

[a] Electronic Ceramics Department, Jožef Stefan Institute, Jamova cesta 39, 1000 Ljubljana, Slovenia. E-mail: tadej.rojac@ijs.si; Tel: +386 1 477 3834
[b] Faculty of Physics, Vilnius University, Saulėtekio al. 9, 10222 Vilnius, Lithuania
[c] Jožef Stefan International Postgraduate School, Jamova cesta 39, 1000 Ljubljana, Slovenia

† Electronic supplementary information (ESI) available. See DOI: 10.1039/d0tc05854h

ordering was suggested to play a role in the distribution of oxygen vacancies inside the material, affecting the pinning behavior.[8,9]

Acceptor doping in ferroelectrics and relaxor ferroelectrics has also been used for tailoring the electrocaloric (EC) response. This is particularly important because the hardening-induced low losses are highly desired in EC applications due to reduced self-heating effects and lowered energy consumption.[13,14] In addition, defect complexes can affect the EC response. This was, *e.g.*, studied by Ma *et al.*[15] in modified $BaTiO_3$ by Monte-Carlo simulations. Their results showed that the EC effect can be substantially increased in the presence of defect-related dipoles when these dipoles lie parallel to the external electric field. The model, however, assumes fixed defect dipoles whose orientation is unaffected by the large applied electric fields. This is not consistent with the experimental observations on acceptor-doped PZT where a dynamic reorientation of the defect dipoles was found to occur during the EC field cycling.[16] In addition, Grünebohm *et al.*[17] studied the influence of doping and the associated defects on the EC properties of $BaTiO_3$ by molecular dynamic simulations. They showed that the local defect dipoles with slow relaxation times in $BaTiO_3$ do not only slightly reduce the EC effect, but also broaden and shift the maximum ΔT_{EC} response towards higher temperatures. Finally, experimental data by Molin *et al.*[18] showed the influence of Mn doping on the dielectric and EC properties of PMN-8PT ceramics. Compared to the undoped material, Mn doping resulted in a significantly decreased dielectric loss tangent, while a slight reduction of EC properties was observed. Despite systematically evaluating a wide range of dopants, including Mn, the study of Molin *et al.*[18] does not provide any mechanistic explanations for the observed effects of the Mn dopant on properties nor does it support the presumed effects of the mentioned Mn-dopant-compensated oxygen vacancies.

Here, we investigate the effect of acceptor (Mn) doping on the broadband dielectric permittivity, high-field *P–E* hysteresis and EC response of PMN-10PT relaxor ferroelectric material, a composition that has recently been shown to be a promising candidate for EC refrigeration.[19] The effect of Mn doping shows up in the core relaxor feature of this material, *i.e.*, in the frequency dispersion of the permittivity maximum. The suppression of both the magnitude of the permittivity peak and its frequency dispersion suggests marked pinning effects arising from the presence of oxygen-vacancy-related defect complexes. This pinning is also reflected in the *P–E* hysteresis loops, showing pinching behaviour, typical for acceptor-doped hard ferroelectrics. The pinning effect of the defect complexes is indirectly confirmed by quenching experiments and thus by the transition from the aged to the de-aged state of the sample. From the EC perspective, Mn-doped samples exhibit a broader EC maximum as a function of temperature, making Mn-doped PMN-10PT suitable for EC use in a wider temperature range. Using temperature-dependent pyroelectric measurements, we explain this EC behaviour by the observed shift of the freezing point towards lower temperatures in the doped samples. We believe that the results of this work can be useful for further investigation of defect engineering of relaxor ferroelectrics aiming at improved functional responses.

Experimental

$0.9Pb(Mg_{1/3}Nb_{2/3})O_3$–$0.1PbTiO_3$ (PMN-10PT) ceramics were prepared by substituting the B-site ions (in their appropriate molar ratios set by the nominal PMN-10PT formula) with 0.5 and 1 mol% Mn. For reference, undoped ceramics were also prepared. From here on, the PMN-10PT samples without and with 0.5 and 1.0 mol% Mn are denoted as undoped, Mn-0.5 and Mn-1.0, respectively.

Ceramic powders were prepared from constituent oxides, all from Sigma Aldrich, *i.e.*, PbO (99.99%), MgO (99.95%), Nb_2O_5 (99.9%), TiO_2 (99.8%) and MnO_2 (99.9%). Prior to synthesis, the MgO and MnO_2 powders were milled in an attritor mill (Netzsch, PE 075/PR 01) at 600 min^{-1} of rotational frequency for 3 h to reduce the particle size. Powders of PbO, Nb_2O_5 and TiO_2 were used as received. In the first step of the synthesis, $PbTiO_3$ was prepared from the homogenized PbO–TiO_2 powder mixture by calcination at 750 °C for 2 h. The heating and cooling rates were 5 °C min^{-1}. For the synthesis of the Mn-0.5 and Mn-1.0 powders, MgO, Nb_2O_5 and MnO_2 were added to the pre-synthesized $PbTiO_3$ and mixed in the appropriate stoichiometric molar ratio. The same procedure was used for the undoped samples. The homogenized powder mixture was then high-energy milled in a planetary mill (Retsch, PM 400) at 300 min^{-1} up to 80 h, similarly as reported in ref. 20 and 21. The high-energy milled powders were finally milled in an attritor at 800 min^{-1} for 4 h in isopropanol.

The phase composition of the powders was analysed by X-ray diffraction (XRD) analysis using an X-ray diffractometer with Cu-Kα1 radiation (X'Pert PRO MPD, PANalytical, Almelo). The XRD patterns were recorded in the 2θ-range from 10° to 70° using a 1D detector (X'Celerator, PANalytical, Almelo) with a capture angle of 2.122°. The exposure time for each step was 100 s and the 2θ-interval between the obtained data points was 0.034°. The XRD pattern of the as-synthesized powder corresponded to the perovskite phase only (see the ESI,† Fig. S1). The average particle size and particle size distribution, determined by a light-scattering technique (Microtrac S3500), are shown in the ESI,† Fig. S2.

In the next step, the powder compacts were pressed uniaxially at 50 MPa and then isostatically at 300 MPa, followed by sintering at 1200 °C for 2 h in double alumina crucibles in air and in the presence of a PMN-10PT packing powder of the same composition as the pellets. The heating and cooling rates were 2 °C min^{-1}. The sintering behavior of the powders is reported in the ESI,† Fig. S3. The XRD patterns of the crushed pellets were recorded under the same conditions as described earlier. In ceramics, only the perovskite phase was detected (see the ESI,† Fig. S4). The densities of the sintered ceramics were measured with a gas-displacement density analyser (Micromeritics, AccuPyc III 1340 Pycnometer).

For the microstructural investigations with a field-emission scanning electron microscope (FE-SEM; JEOL JSM-7600), equipped with energy- and wavelength-dispersive X-ray spectrometers (EDXS and WDXS, respectively), the ceramic samples were cut with a diamond wire saw, polished to a 0.25 μm finish and, in the case of the grain-size analysis, thermally etched at ~300 °C below the sintering temperature (*i.e.*, at 900 °C). Prior to analyses with FE-SEM, the sample was coated with a 4 nm-thick carbon coating in a Gatan PECS 682 to provide surface electrical conduction and thus avoid charging effects. For the stereological analysis, more than 300 grains per sample were analysed using the Image Tool software.[22] The grain size is expressed as the Feret's diameter.[23] The results of the microstructural analyses are collected in the ESI,† Fig. S5 (FE-SEM images) and Fig. S6 (grain size distribution histograms).

Continuous-wave electron paramagnetic resonance (EPR) measurements were performed using a conventional X-band Bruker ELEXYS E580 EPR spectrometer operating at 9.8 GHz and equipped with a standard rectangular TE102 cavity. The strength and frequency of the modulating field were 5 G and 100 kHz, respectively. A variable nitrogen temperature control system was used to vary the temperature. Spectral simulations were performed using the EasySpin 5.2.20 software.[24]

For the electrical measurements, the sintered pellets of ~6 mm in diameter were first cut and polished clean in organic solvents, as reported in ref. 25. Two set of samples were prepared, *i.e.*, for dielectric measurements (sample set A) and *P*–*E* and EC measurements (sample set B). Pellets from set A were covered on each surface side with silver paint (Hans Wolbring GmbH). Samples from set B used Cr/Au electrodes in the shape of a circle with diameters equal to 5 mm deposited on the pellet surfaces by RF-magnetron sputtering (5 Pascal).

The aging state of the samples was set by the annealing procedure performed prior to every measurement. The annealing was performed either at 500 °C for 2 hours with a heating rate of 5 K min^{-1} (sample set A) or 600 °C for 1 hour with a heating rate of 2 K min^{-1} (sample set B). Since the aging state is set during cooling from these temperatures down to the room temperature, comparable aging conditions were provided by using the same cooling rate of ~1 K min^{-1} in all cases.

Linear dielectric data in the temperature range from −140 °C to 180 °C were obtained using three different experimental techniques. First, to obtain the complex dielectric permittivity below 1 MHz, the capacitance and loss tangent were measured using an HP 4284A LCR meter. The flat capacitor model was used for the calculation of the complex dielectric permittivity. Second, the frequency range from 1 MHz to 1 GHz was covered by measuring the complex reflection coefficient from the end of the coaxial line.[26] The real and imaginary parts of the dielectric permittivity were obtained from these data. Higher frequency data were corrected according to the multi-mode capacitor model.[27,28] Third, the measurements in the range from 8 to 50 GHz were performed using waveguided systems. The scalar transmission and reflection coefficients were measured from the needle-shaped sample placed in a waveguide that only supports the fundamental H_{10} mode. The samples were placed in the center of the waveguide where the electric field is maximum, while the magnetic field is minimum. The reflection/transmission coefficients were measured with a scalar network analyzer R2400 (Elmika). A detailed description of the method is reported elsewhere.[26,29]

Nonlinear dielectric spectroscopy was performed using a Data Translations DT9834 16 bit DAC/ADC module, which generates a 0 V biased high-quality first harmonic input signal. The amplitude of the alternating electric field on the sample was ~0.15 kV cm^{-1}, which is well below the coercive field of the material. The electric current generated by the sample was converted to the voltage signal by the current pre-amplifier Stanford Research Systems SR570. Temperature measurements were carried out with a 4 W-RTD Pt-100 temperature sensor connected to a Keithley Integra 2700 digital multimeter.

Current–voltage curves were measured at room temperature on ~200 μm-thick ceramic samples using a Keithley 237 Source-Measure Unit. During the measurements, a step-like electric signal was used. The length of the individual step was 30 min so that the current achieved a stable value and thus only the time-independent current (leakage current) was recorded and plotted against the electric field. Every 30 min, the electric field was increased in steps of 1 kV cm^{-1} up to 10 kV cm^{-1} and in steps of 5 kV cm^{-1} from 10 to 30 kV cm^{-1}.

For *P*–*E* measurements, an Aixacct TF analyser 2000 was used. The measurements were performed in silicon oil at 25 °C on samples with a thickness of 200 ± 20 μm. The frequency was kept constant at 1 Hz, while the sinusoidal electric fields of magnitude of 20 kV cm^{-1} and 50 kV cm^{-1} were applied to the samples. The pyroelectric effect was measured using the same measurement system; in this case, the samples were poled prior to the pyroelectric characterization with a triangular pulse of 30 kV cm^{-1} at 10 Hz. The heating rate of 10 K min^{-1} was used to measure the response in the temperature range from −73 °C (200 K) to 57 °C (330 K).

Quenching experiments were performed first by heating a ~200 μm-thick ceramic sample with electrodes in a furnace tube to 400 °C (well above the dispersive permittivity maximum, which is for the undoped PMN-10PT close to room temperature[21]). The heating rate was 10 °C min^{-1}. After exposing the sample for 30 min at this temperature, the sample was quenched by dropping it into liquid nitrogen (within 5 seconds). After quenching, the sample was rapidly (within less than 3 seconds) inserted into a precooled (−50 °C) sample holder of the Aixacct TF analyser 2000 in order to measure *P*–*E* loops immediately. No evidence of cracks and change in the sample mass was observed after quenching.

Direct EC measurements were performed on ~80 μm-thick samples in a modified high-resolution calorimeter (Netzsch DSC 204 F1), which was used for temperature regulation. The EC signal was measured with a bead thermistor attached to the samples. The electrical signal was established with a Keithley High Voltage Source-Measure Unit 237 and the thermistor resistance was obtained with a digital multimeter (Keithley

2100). The corrected EC temperature change, T_{EC}, was calculated using the below equation:[30]

$$\Delta T_{EC} = \Delta T_{meas} k = \Delta T_{meas} \frac{\sum_i m^i c_E^i}{m^a c_E^a} \quad (1)$$

where T_{meas} is the actual measured temperature change, k is the correction factor, m^i and c_E^i are the mass and specific heat capacity for each of the inactive components (thermistor, sample without electrode, glue and electrical wires), respectively, and m^a and c_E^a are the mass and specific heat capacity for the active material (sample with the electrodes), respectively. The calculated k was $\sim$1.7 for all samples.

Results and discussion

We first present the results of the X-band continuous-wave EPR measurements, the purpose of which was to probe the defect chemistry related to the oxidation state of the Mn ions in PMN-10PT doped with 0.5% and 1% Mn. The room-temperature EPR spectra of these two compositions in Fig. 1 reveal typical powder patterns of the paramagnetic Mn ions in a slightly disordered environment.[31] The spectral lines of the Mn-1.0 sample are slightly broader than those of the Mn-0.5 sample due to the stronger magnetic dipolar interactions between the Mn centers. The temperature-dependent EPR measurements of PMN-10PT doped with 0.5% Mn, shown in the ESI,† Fig. S7, do not indicate any significant changes in the local chemical environment of the Mn ions in the temperature range between −145 °C and 65 °C.

EPR spectroscopy can be used to determine the oxidation state of the Mn ions. In the case of Mn^{2+} ions, the expected g-factor should be slightly higher than 2, while for Mn^{4+} ions

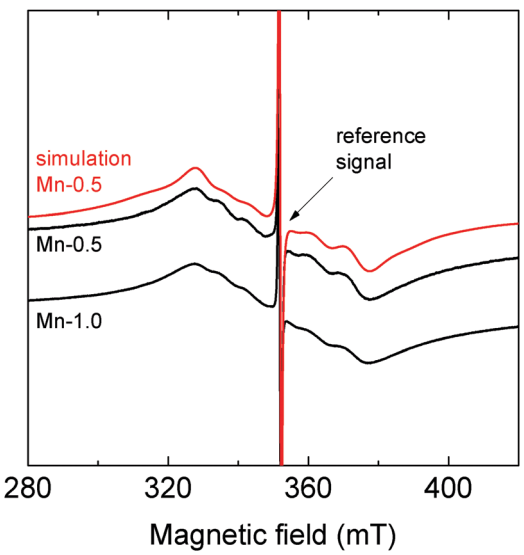

Fig. 1 Room-temperature X-band continuous-wave EPR spectra of PMN-10PT doped with 0.5% and 1% Mn. The simulated spectrum is shown in red (see the main text for details). The sharp line originates from the coal reference sample with g = 2.003085.

$g < 2$.[31] The observed EPR spectra of the Mn-0.5 and Mn-1.0 ceramics display a pronounced broadening due to the distribution of the zero-field splitting, which makes it difficult to accurately determine the g-factor.[31] Nevertheless, we performed spectral simulations of the Mn-0.5 spectrum using the diagonalization of the spin Hamiltonian, which takes into account the electron Zeeman interaction, hyperfine interaction and zero-field splitting along with its distribution.[31] The simulations were performed by taking into account a known reference signal of a coal sample (see the sharp lines in Fig. 1). The obtained g-factor of the Mn centers in the Mn-0.5 sample is $g = 2.0008 \pm 0.0007$, which likely indicates the predominant presence of Mn^{2+} ions. Due to the uncertainty of the determined g-factor, however, we cannot completely rule out the possibility of a minor presence of Mn^{4+} ions. We also cannot discard the scenario where a fraction of the Mn centers is Mn^{3+} ions, which in the low-spin state are diamagnetic, while in the high-spin state might be EPR silent at X-band frequency due to a very large zero-field splitting. Unfortunately, we were unable to accurately simulate the line broadening of the Mn-1.0 EPR spectrum to determine the g-factor for this composition; however, due to the same sintering conditions (see the 'experimental' section) and a small difference in the dopant concentration, one may expect a similar Mn oxidation state in the two doped samples.

The presence of Mn^{2+} ions, as indicated by EPR, on the nominal B^{4+} sites in PMN-PT confirms that the Mn acts as an acceptor, *i.e.*, Mn_B'' (in Vink–Kroger notation), which by compensation with oxygen vacancies $(V_O^{\bullet\bullet})$ should bind into the defect complexes of the acceptor-center-oxygen-vacancy type,[7] *i.e.*, $Mn_B''-V_O^{\bullet\bullet}$. The presence of Mn^{2+} ions with the acceptor character and the associated $Mn_B''-V_O^{\bullet\bullet}$ defect complexes in our doped ceramics is strongly supported by the previous studies on the Mn-doped PMN-PT and similar relaxor ferroelectric single crystals.[32–35] In particular, the $Mn_B''-V_O^{\bullet\bullet}$ complexes have also been directly identified in the Mn-doped PMN-PT[34] and $BaTiO_3$[36] by spectroscopy analysis. An indirect but strong support to the presence of such complexes in our doped samples is given by the pinched P–E hysteresis loop of the Mn-doped PMN-10PT, presented at the later stage of this report. As will be explained, these data suggest the presence of not only such defect complexes but also their strong pinning effects; the pinning effects are analyzed next using broadband dielectric spectroscopy.

The temperature dependence of the real part ($\varepsilon'(T)$) of the complex dielectric permittivity ($\varepsilon^*(T)$) of the undoped, Mn-0.5 and Mn-1.0 PMN-10PT is shown in Fig. 2(a–c). The undoped PMN-10PT (Fig. 2a) shows clear features of relaxor behaviour, namely, the maximum $\varepsilon'(T)$ decreases in magnitude with increasing driving frequency, shifting towards higher temperatures. These relaxor features are strongly altered by the Mn doping. The first observation is the strong reduction of the maximum of the permittivity (Fig. 2(b and c)). While such reduction has already been reported,[37–40] our analysis reveals further important details. In both the doped PMN-10PT ceramics (Fig. 2b and c), the shift of the $\varepsilon'(T)$ maximum and the decrease in its intensity with increasing frequency are only observed at higher frequencies ($f > 1$ MHz in Mn-0.5 and $f > 18$ MHz in

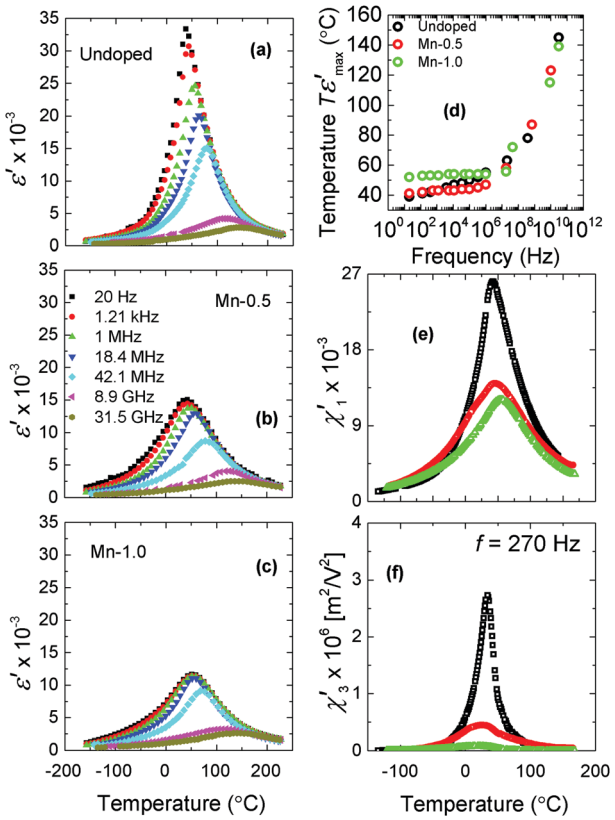

Fig. 2 Temperature dependence of dielectric permittivity, measured at different frequencies (ranging from 20 Hz to 31.5 GHz), of the (a) undoped, (b) Mn-0.5 and (c) Mn-1.0 ceramics. (d) Temperature of the maximum permittivity plotted as a function of frequency for undoped, Mn-0.5 and Mn-1.0 as extracted from the data shown in panels (a–c). (e) First-order and (f) third-order susceptibility compared among the three samples investigated (frequency 270 Hz).

Mn-1.0). The effect of doping on the frequency dispersion of the permittivity maximum is more obvious in Fig. 2d, which shows the extracted temperatures of the maximum $\varepsilon'(T)$ as a function of frequency for the three samples. This result suggests a suppression of the low-frequency (sub-MHz) dynamics related to the relaxor behavior already with a small amount of Mn, *i.e.*, 0.5% (Fig. 2d, compare red with black open circles). Also note that with a further addition of 1% Mn, the response is practically frequency independent in the sub-MHz range (see the low-frequency plateau in the green data in Fig. 2d).

Fig. 2(e and f) shows the comparison of the first- and the third-order susceptibility maxima (χ'_1 and χ'_3, respectively) for the undoped, Mn-0.5 and Mn-1.0 ceramics (these data are shown for 270 Hz; the complete dataset as a function frequency for the three samples is reported in the ESI,† Fig. S8). A reduction of the maxima with Mn doping is observed, which is more evident in the third-order susceptibility where the χ'_3 peak in Mn-1.0 is almost totally suppressed (precisely, by 97% relative to the undoped χ'_3 maximum value; see Fig. 2f, green curve). In addition, the nonlinear susceptibility $\chi'_3(T)$ of all the PMN-10PT samples is positive in the whole measured temperature range. This is consistent with the behavior of the classical relaxor ferroelectric PMN single crystal where the spontaneous structural phase transition is absent.[41,42] In contrast, Dkhil *et al.*[43] reported on a structural phase transition into a rhombohedral phase in PMN-10PT at $T_C \approx 285$ K using X-ray diffraction. Our data do not confirm this scenario and are thus consistent with the results of the neutron diffraction experiments, which revealed that, unlike in the surface skin layer of the crystal, the phase transition is absent inside the bulk of PMN-10PT.[44]

For the sake of a simplistic explanation of the effect of doping on the linear and nonlinear dielectric permittivity, we consider the well-known temperature-dependent size of PNRs or their correlation,[45–48] which has also been confirmed in PMN by the very recent reversed Monte Carlo studies.[49] In this view, the PNR dynamics slow down as the temperature is decreased and the frequency dispersion of the permittivity maximum is observed as a result of larger correlations between the PNRs following progressively lower driving field frequencies with decreasing temperature.[50,51] The Mn doping affects the temperature dependence of permittivity in two ways. First, the doping-induced reduction of χ'_1 (Fig. 2e) and, in particular, χ'_3 maxima (Fig. 2f), which is more sensitive to the dipolar order than the linear part,[42] shows that the dynamic features of PMN-10PT are suppressed. Second, as opposed to undoped PMN-10PT, an almost complete absence of the frequency dispersion of the permittivity maximum is observed in the low-frequency (sub-MHz) range in the doped samples (Fig. 2d). This indicates that in these doped samples, the largest polar entities are either smaller (or they correlate on a shorter scale) than those in the undoped ceramics or they are pinned and thus static. Since their dynamic contribution is much lower in the doped samples, the dispersion appears only at the microwave frequencies (above 40 MHz). It is important to note that the dielectric properties in the 9–30 GHz frequency band are very much alike in all three samples, supporting the idea that the smaller polar entities have similar dynamics irrespective of the added dopant.

As suggested by the EPR data in Fig. 1, the obvious candidates responsible for the pinning and reduced PNR dynamics are the $Mn''_B-V^{\bullet\bullet}_O$ defect complexes. Such complexes are re-orientable *via* $V^{\bullet\bullet}_O$ hopping over adjacent oxygen sites inside the perovskite oxygen octahedra with the preferred orientation in the aged state dictated by the polarization in the material. To explain the observed dielectric features induced by doping (Fig. 2), we therefore suggest a similar scenario to that in normal (non-relaxor) ferroelectrics in which case complexes align in the direction of spontaneous polarization, pinning the domain walls.[4] Eventually, PNRs in PMN-10PT can be strongly electrostatically and elastically pinned by the $Mn''_B-V^{\bullet\bullet}_O$, resulting in static polar regions, which is macroscopically reflected in a suppressed low-frequency permittivity dispersion. To be noted is that the mechanism of PNR pinning by defects is consistent with the results of a previous study on aging effects in Mn-doped PMN-10PT ceramics.[52] Unlike in that study, however, we have not observed double peaks in the temperature-dependent dielectric permittivity, which could be explained by the different aging

procedures, *i.e.*, in our case aging was set by the annealing performed prior to dielectric measurements (see the 'Experimental' section), while in that study controlled aging experiments were performed at various temperatures for up to ~40 days of aging time.

In the next step, we analyze the effect of $Mn''_B-V^{\bullet\bullet}_O$ defect complexes on the ferroelectric ordering in terms of the ergodic-to-non-ergodic phase transition at the so-called freezing temperature, T_f. For T_f analysis, we use pyroelectric measurements. Fig. 3 presents the temperature dependence of the pyroelectric coefficients of all three studied compositions (undoped, Mn-0.5, and Mn-1.0). The samples were first cooled down to −73 °C where an electric field was applied to the samples, inducing a poled ferroelectric state (see the 'Experimental' section for details). Upon heating, a peak in the pyroelectric coefficients was observed in all three compositions: in undoped PMN-10PT the peak appeared at 21 °C (black curve), in Mn-0.5 at −26 °C (red curve), and in Mn-1.0 at −28 °C (blue curve). It was shown previously that the peak in the pyroelectric current in the poled relaxor ferroelectric materials corresponds to T_f.[53] The data therefore suggest a reduction of T_f by Mn doping of almost 50 °C. Note that most of the T_f reduction is obtained with 0.5% of Mn, suggesting that already a small concentration of the defect complexes has a significant effect on the T_f and thus on the non-ergodic ferroelectric ordering. In addition to providing the pinning effects to PNRs, as indirectly observed from the permittivity behavior (Fig. 2), the introduced defects also suppress the interaction between PNRs and/or affect their growth, making the long-range ferroelectric order more difficult to evolve as the material is cooled, hence the T_f is lowered by doping. This mechanism could be somewhat similar to that proposed for "hard" PZT where the acceptor-$V^{\bullet\bullet}_O$ defect complexes are thought to be responsible for the disruption of the spontaneous polarization, resulting in a finely fragmented nanodomain structure.[54] We find here that the acceptor (Mn) doping is a valuable method for controlling simultaneously the frequency dispersion of permittivity and the stability of the ergodic phase. As it will be shown in the following analyses, this has profound effects on the high-field polarization hysteresis and EC response.

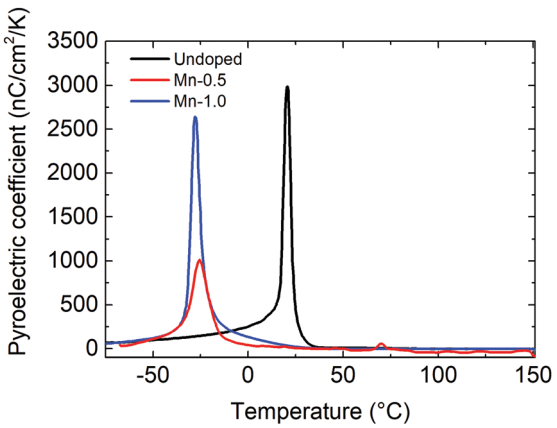

Fig. 3 Temperature dependence of the pyroelectric coefficient for the analysed compositions. The black, red and blue curves correspond to the undoped, Mn-0.5 and Mn-1.0 samples, respectively, as noted on the plot.

We continue by showing the effect of the Mn dopant on the high-field polarization response. The *P–E* hysteresis loops of the undoped and Mn-doped samples measured at RT and at two different field amplitudes are shown in Fig. 4a and b with the corresponding *j–E* hysteresis loops displayed in Fig. 4c and d. All the samples exhibit slim *P–E* loops, typical for the relaxors in the ergodic phase. While a pinched *P–E* loop shape is visible only in the two doped samples (red and blue loops in Fig. 4a and b), the *j–E* hysteresis confirms its presence in the undoped sample. The pinched shape is more visible by inspecting the *j–E* hysteresis because the double current peaks for both the positive and the negative polarities of the applied field, responsible for the pinched shape, can be identified in all the samples in Fig. 4c and d.[55] Nevertheless, the effect of Mn doping on the pinched hysteresis is evident in the *P–E* loops, *i.e.*, the Mn-doped samples exhibit a more pronounced pinching, a smaller hysteresis and a more "canted" loop shape in comparison with the undoped sample (compare black with red and blue loops in Fig. 4a and b); these differences are also reflected in broader current peaks of the doped samples, as compared to those of the undoped PMN-10PT (Fig. 4c and d). The pinched *P–E* loops, like those shown in Fig. 4a and b for the Mn-doped PMN-10PT, were also previously observed in the Mn-doped PMN-8PT ceramics.[18] Furthermore, the comparison of the loops measured at different field amplitudes (Fig. 4a *vs.* Fig. 4b) shows that at the lower field of 20 kV cm^{-1}, the maximum polarization (P_{max}) systematically decreases with the increasing concentration of Mn (Fig. 4a), while at the electric field of >35 kV cm^{-1}, the P_{max} becomes comparable (~29 μC cm^{-2}) (Fig. 4b) and reaches saturation.

The origin of the pinched *P–E* hysteresis loops can be in principle related to the (i) presence of antiferroelectric phase, which, by applying the electric field, reversibly transforms into a ferroelectric phase,[55,56] (ii) coexistence of the polar and non-polar phases, which reversibly switch by applying the electric field: an example is the well-known relaxor-to-ferroelectric field-induced transformation,[57–60] and/or (iii) presence of charged defect complexes of the acceptor-oxygen-vacancy type, such as $Mn''_B-V^{\bullet\bullet}_O$,[61] which stabilize the (pin) domain walls, giving rise to a restoring force by applying the electric field and thus pinched loop shape. Antiferroelectric distortions (hypothesis (i)) have been previously discussed in PMN[62,63] and PMN-PT,[64] meaning that their effects on the *P–E* loops cannot be completely excluded. Next, the critical point of the PMN-10PT is in the vicinity of room temperature,[65] therefore, it is possible that the loop is at least in part pinched due to the reversible transition between the relaxor and the ferroelectric phase (hypothesis (ii)), as extensively discussed for PMN[66] and similar relaxor materials.[59,67]

To further check for hypothesis (iii), the *P–E* loops were measured below the freezing point, *i.e.*, sufficiently below room temperature,[68] thus in the non-ergodic phase region where the ferroelectric phase can be permanently induced by the application of strong electric fields. In particular, we were interested in

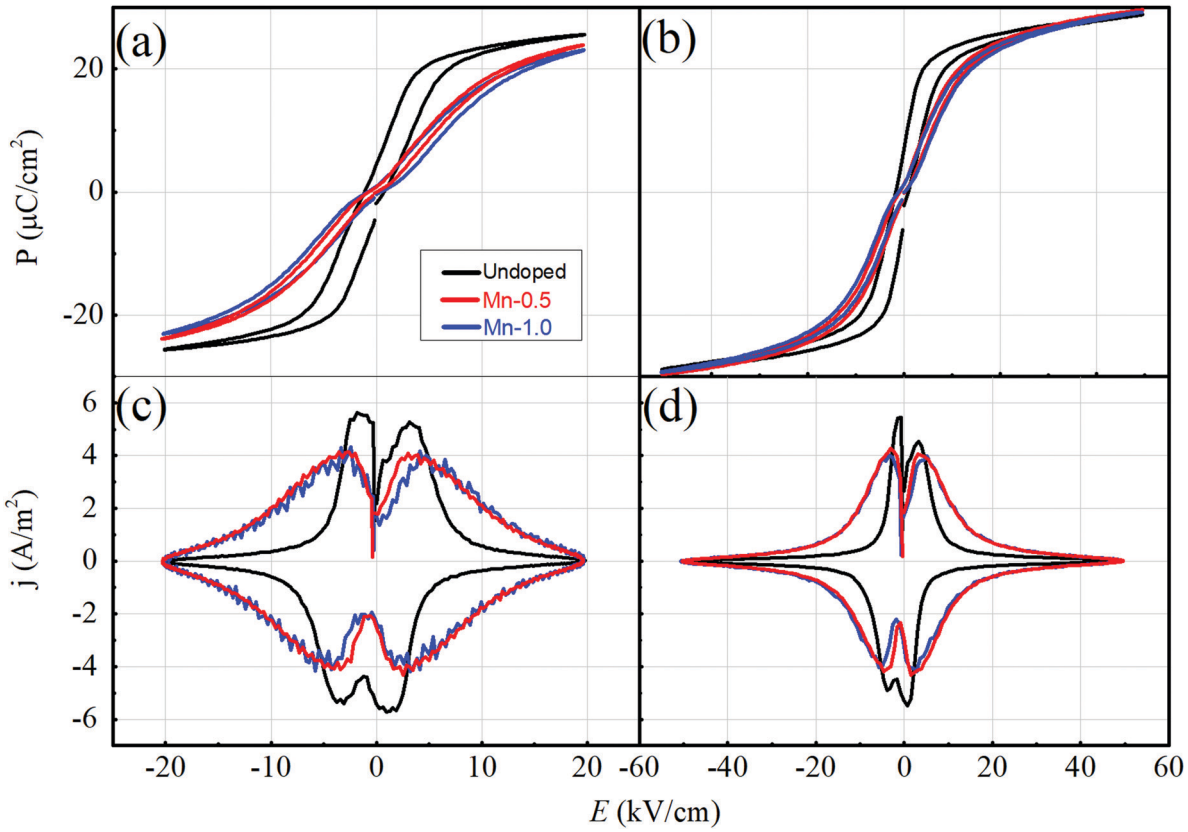

Fig. 4 *P–E* hysteresis loops of the undoped, and 0.5% and 1% Mn-doped PMN-10PT measured at (a) 20 kV cm^{-1} and (b) 50 kV cm^{-1} of the field amplitude. The corresponding electric-current density (*j*) *versus* electric field (*E*) hysteresis loops measured at 20 kV cm^{-1} and 50 kV cm^{-1} are shown in panels (c) and (d), respectively.

whether the pronounced pinching behaviour in the Mn-doped samples observed at room temperature (Fig. 4a and b) would be also identified in the non-ergodic ferroelectric phase at low temperatures, as expected if the pinching is dominated by the defect pinning mechanism (hypothesis (iii)).

Fig. 5 shows the *P–E* loops of the undoped and Mn-1.0-doped PMN-10PT recorded in the temperature range from −50 °C to 100 °C. Consistent with the determined T_f (Fig. 3), at −50 °C both the samples display a wide hysteresis due to the field-induced long-range ferroelectric order in the PMN-PT system (blue loops in Fig. 5a and b).[69,70] In strong contrast to the undoped sample, exhibiting an opened and a square-like *P–E* loop (Fig. 5a, blue loop), the *P–E* loop of Mn-1.0 is evidently pinched (Fig. 5b, blue loop). The pinched hysteresis loops in

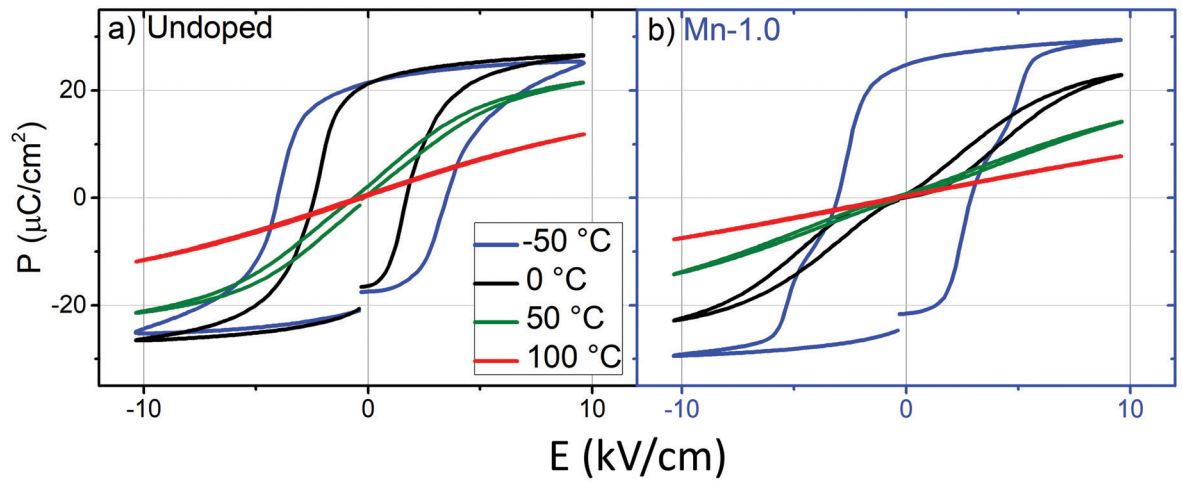

Fig. 5 *P–E* hysteresis loops measured at different temperatures for the (a) undoped and (b) 1% Mn-doped PMN-10PT.

the Mn-doped samples are thus consistent with the predominant pinning effects mediated by the $Mn''_B-V^{\bullet\bullet}_O$ complexes (hypothesis (iii)) as already suggested by the frequency and temperature-dependent dielectric permittivity (Fig. 2).

As the temperature is increased, the *P–E* response of both samples becomes gradually slimmer until 100 °C where the response is quasi-linear and anhysteretic, reflecting the expected transition from the non-ergodic to the ergodic phase with increasing temperature. Interestingly, while the *P–E* loop of the undoped sample at 0 °C is still wide and open (black loop in Fig. 5a), a response typical in the ferroelectric phase region, it is much slimmer and obviously pinched in the Mn-doped PMN-10PT (black loop in Fig. 5b), indicating the presence of the ergodic phase in the doped sample at 0 °C. This *P–E* behavior is in agreement with the downward shift of the T_f by Mn doping, *i.e.*, according to the data shown in Fig. 3, at 0 °C the undoped PMN-10PT should be in the non-ergodic state (wide hysteresis) while the doped PMN-10PT is still in the ergodic state (slim hysteresis).

A way to find out whether the pinched loop in the ferroelectric phase of the Mn-doped PMN-10PT (Fig. 5b, blue loop) is indeed dominated by the defect-mediated domain-wall pinning effects is to perform quenching experiments. As explained in previous studies,[2,71,72] the domain walls can be depinned from the defects by rearranging the originally ordered defects, which are aligned along with the spontaneous polarization, into a disordered state. In non-relaxor ferroelectrics, this can be done by heating the ceramics above the Curie (T_C) temperature in the paraelectric state where the charged defects become disordered due to the absence of the spontaneous polarization. The ceramic is then quenched from this high temperature to below T_c, typically to room temperature. Fast cooling prevents oxygen vacancies to diffuse from the disordered state back to the equilibrium ordered positions, hence, the disordered state becomes frozen at low temperatures. The obtained disordered defect state releases locally the domain walls from the strong pinning, which was originally mediated by the ordered defects, thus opening up (depinching) the *P–E* loop.[72]

In the analogy to ''normal'' (non-relaxor) ferroelectrics, quenching experiments were utilized here on the PMN-10PT relaxor material. Note that in order to preserve the metastable disordered state and prevent aging (defect ordering), quenching was performed by dropping the sample into liquid nitrogen (thus to a temperature below T_f), and then the sample was, in a matter of a few seconds, transferred to a pre-cooled sample holder (−50 °C) where the *P–E* loops were measured (see the 'Experimental' section for further details). The *P–E* loops of the Mn-1.0 sample, measured at −50 °C, before (as-sintered) and after quenching are shown in Fig. 6. In contrast to the as-sintered sample, which is characterized by a pinched loop, the hysteresis of the quenched sample shows no evidence of pinching. The difference between the two behaviors is more evident in the *j–E* curves (Fig. 6, dashed curves), where the double current peak measured in the as-sintered sample merges into a single peak due to depinching.[55]

The clear depinching of the loop by quenching strongly suggests that the original pinched shape of the loop of the

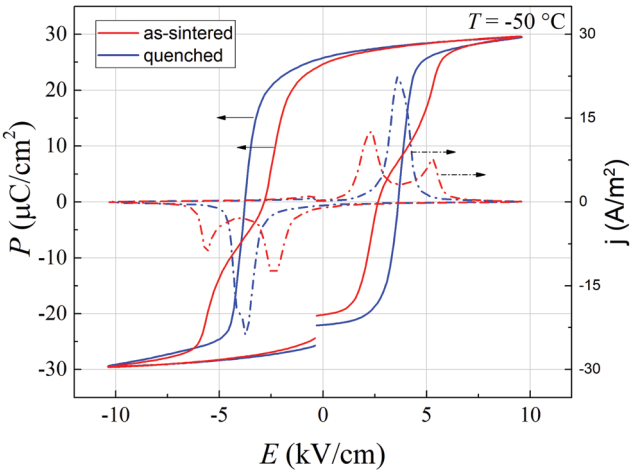

Fig. 6 *P–E* (full curves) and *j–E* (dashed curves) hysteresis loops of as-sintered (red) and quenched (blue) 1% Mn-doped PMN-10PT, measured at −50 °C.

as-sintered Mn-doped samples in the ferroelectric phase is dominated by charged point defects, most likely the $Mn''_B-V^{\bullet\bullet}_O$ defect complexes as suggested by the EPR analysis (Fig. 1) and literature data.[33–35] Note that the characteristic double current peak as shown in Fig. 6 (red-dashed curve), where the double peak appears positive for the positive field polarity and negative for the negative field polarity, suggests inhomogeneous domain switching, possibly related to inhomogeneous defect distribution as suggested by Schenk *et al.*[73] Finally, the de-aging observed here by quenching is consistent with the de-aging by AC field cycling previously observed in Mn-doped PMN-10PT.[52]

Next, we investigate the effect of the defect complexes, associated with the introduced Mn dopant, on the EC response of the PMN-10PT. The results of the direct EC measurements of the undoped, Mn-0.5 and Mn-1.0 samples are shown in Fig. 7. Note that the investigated samples withstood electric fields higher than 70 kV cm^{-1} without experiencing a dielectric breakdown; however, for the sake of the EC study, the results of ΔT_{EC} are shown for the electric fields up to 70 kV cm^{-1}. In addition, Joule heating in all the samples and at all the measured electric fields and temperatures was negligibly small (<0.05 K) during the direct EC measurement. This is consistent with the *I–V* measurements (not shown here) where leakage currents measured up to 30 kV cm^{-1} were below the limit of the measurement system, *i.e.*, <1 pA.

Inspection of the results of the EC measurements in Fig. 7 reveals the following observations. First, the undoped sample exhibits the largest ΔT_{EC} of 1.76 K, measured at 70 kV cm^{-1} and 80 °C. This is in good agreement with the values reported previously[74] for columbite-derived PMN-10PT ceramics. Peräntie *et al.*[74] directly measured ΔT_{EC} of 1.19 K at 50 kV cm^{-1} and 89 °C, while the undoped sample from Fig. 7 exhibits ΔT_{EC} of 1.28 K at the same field and 91 °C. The small difference in the ΔT_{EC} values could be related to the different microstructures of the samples (*e.g.* density and grain size)[21] or to the different measurement

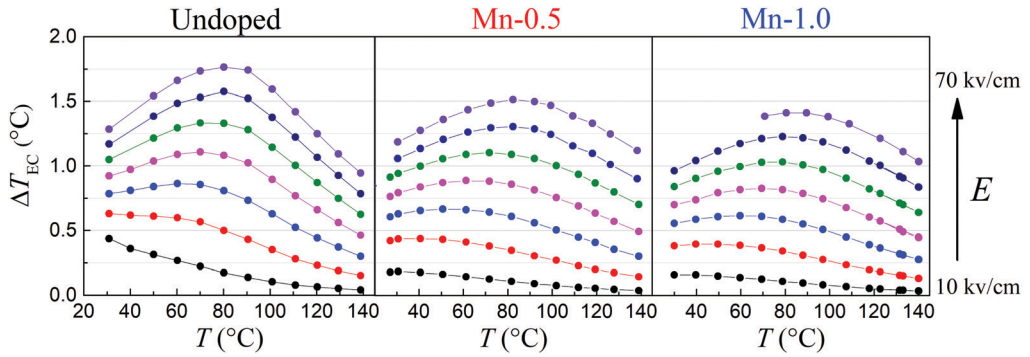

Fig. 7 ΔT_{EC} of the undoped, and 0.5% and 1% Mn-doped PMN-10PT as a function of temperature. The upward pointing arrow on the right-hand side of the figures indicates the increase in the electric field from 10 kV cm^{-1} to 70 kV cm^{-1} with a step of 10 kV cm^{-1}. The dashed curved arrows indicate the upward temperature shift of the maximum ΔT_{EC} in the doped samples. Note that the lines are drawn as a guide to the eye.

setups and used protocols and correction factors.[75] Second, with increasing Mn-concentration, the peak in the EC response as a function of temperature gradually decreases, and it becomes broader and experiences an upward temperature shift (see the curved dashed arrows in Fig. 7). For example, with increasing Mn concentration at 70 kV cm^{-1}, the ΔT_{EC} peak decreases from 1.76 K (undoped) to 1.51 K (0.5% Mn) and 1.41 K (1% Mn) and shifts from 79 °C (undoped) towards 84 °C (0.5% Mn) and 85 °C (1% Mn). Similar behaviour was observed in ref. 18, where a 3 mol%-Mn-doped PMN-8PT showed a half-reduced ΔT_{EC} maximum with the ΔT_{EC} peak located at 25 °C (higher temperature) as compared to the undoped PMN-8PT. The ΔT_{EC} maximum, which is reduced, broadened and shifted towards higher temperatures in the presence of polar defects, was also predicted by simulations on $BaTiO_3$.[17] We note that the Mn-doped samples from our study could potentially exhibit a reduced ΔT_{EC}, with respect to the undoped sample, due to the presence of the low-polarizable intergranular phase, detected in these samples (see the ESI,† Fig. S5). Nevertheless, even though the Mn dopant lowers the overall EC effect of the PMN-10PT material, the ΔT_{EC} values at higher temperatures are even larger in the Mn-doped samples due to the shifted and broadened $\Delta T_{EC}(T)$ curve (compare the ΔT_{EC} values at >120 °C in Fig. 7).

The three phenomena (EC magnitude decrease, and EC peak broadening and shift) observed in the EC response due to Mn doping can be explained by a careful inspection of the electric-field–temperature (E–T) phase diagram of PMN-10PT.[58,65,68] The first consideration is that the doped samples are deeper in the ergodic state when analysed in the temperature range between 30 °C and 140 °C due to their lower T_f. Second, in the ergodic state, a peak in the EC response is expected when crossing the Widom line, which becomes more and more diffused and less pronounced as the temperature is increased further away from the T_f.[76,77] From this reasoning, we can thus suggest that the Mn doping in PMN-10PT results in a diffuse temperature-dependent EC response due to the doping-related lowered T_f. A schematic representation of this effect is depicted in Fig. 8. Since the PNR dynamics have a strong effect on the polarization of the material, which is phenomenologically related to the EC responsivity,[76] the effect of the reduced PNR dynamics on the EC response of the Mn-doped PMN-10PT cannot be ruled out and likely plays a role.

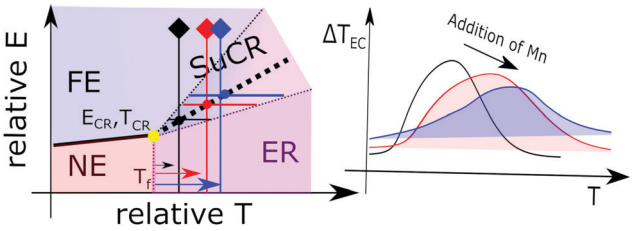

Fig. 8 Schematic illustration of the effect of the proximity of the freezing temperature (T_f) to the temperature-dependent EC response. The left schematic diagram shows a hypothetical E–T phase diagram of the PMN-PT relaxor ferroelectric system with four characteristic phase regions: FE (ferroelectric), NE (non-ergodic), ER (ergodic) and SuCR (supercritical). The diagram was adopted from the experimentally derived E–T diagram of PMN.[69] The onset of the supercritical regime is at the critical point noted by the yellow dot (E_{cr} and T_{cr} denote the critical electric field and critical temperature, respectively). T_f is the freezing temperature and is assumed to lie in close proximity to the T_{cr}. The thick dotted line depicts the Widow line in the supercritical regime close to which a maximum in the EC responsivity is expected as shown in ref. 76. The two thin dotted lines represent the positions of the tails of the EC responsivity away from the Widom line (this behavior was adopted according to the experimental data on PMN, see ref. 78). As seen in the E–T diagram, the EC response becomes wider in the temperature scale (see black, red and blue thick horizontal lines) as the measurement point moves away from the T_f (illustrated with black, red and blue arrows and corresponding vertical lines). In relative terms, the same temperature widening of the EC effect should be observed if the temperature region of the EC measurements is fixed and T_f is progressively lowered. The lowered T_f in the Mn-doped PMN-10PT (see Fig. 3) is thus expected to broaden the temperature dependency of the EC response (ΔT_{EC}), as illustrated in the picture on the right-hand side, along with a shift of the maximum ΔT_{EC} toward higher temperatures. Both these features (broadening, shift) have been confirmed experimentally as a result of Mn doping (see Fig. 7).

Summary and conclusion

In this study, we investigated the acceptor (Mn) doping effects in PMN-10PT on the electrical and electrocaloric properties of this relaxor ferroelectric material. Supported by EPR

spectroscopy, we suggest that the acceptor (Mn) doping introduces defect complexes associated with oxygen vacancy in the material, which have a profound effect on the macroscopic polarization and EC response. Based on the temperature-dependent broadband permittivity studies, the defects provide strong pinning effects to PNRs, suppressing their dynamics. This is reflected in the decreased magnitude of the linear and nonlinear permittivity with doping as well as in the reduced frequency dispersion of the permittivity maximum in the sub-MHz region. As shown by the pinched high-field *P–E* hysteresis loops, the influence of the defect complexes extends from the ergodic to the non-ergodic phase, suggesting a manifestation of the pinning mechanism common to both the short- and the long-range polar order in PMN-10PT. Quenching experiments additionally clarified this picture by showing that the migration of the oxygen vacancies can be kinetically suppressed by rapid cooling, resulting in opened *P–E* loops after quenching. In addition to these pinning effects, the Mn doping was also proposed to locally break the tendency for ferroelectric ordering with decreasing temperature, effectively resulting in the decreased freezing temperature, as confirmed by pyroelectric measurements. The observed broadened peak in the EC effect in the doped samples measured as a function of temperature can be interpreted in terms of the lowered T_f. The results thus show that the defect engineering approach can be efficiently used to tune the stability of the ergodic phase in PMN-PT and thus the temperature behaviour of the EC response of this promising class of materials. In addition, the literature data suggest that this approach may be applied to diverse dopants, not only Mn.[79,80] Finally, the resulting broad and weakly temperature-dependent EC response makes the Mn-doped PMN-10PT a viable cooling element potentially useful for applications requiring broader temperature ranges, such as portable refrigerators and body-worn chillers.

Conflicts of interest

There are no financial or other kind of conflicts to declare.

Acknowledgements

T. R., A. B. and B. M. would like to thank the Slovenian Research Agency for the financial support in the frame of the doctoral project of Andraz Bradesko, project J2-7526, J2-1738, and core funding P2-0105.

Notes and references

1 B. Jaffe, W. R. J. Cook and H. L. Jaffe, *Piezoelectric Ceramics*, Academic Press Inc., London, UK, 1971, vol. 3.
2 D. Damjanovic, *The Science of Hysteresis*, Elsevier, 2006, vol. 3, pp. 337–465.
3 Y. A. Genenko, J. Glaum, M. J. Hoffmann and K. Albe, *Mater. Sci. Eng., B*, 2015, **192**, 52–82.
4 U. Robels and G. Arlt, *J. Appl. Phys.*, 1993, **73**, 3454–3460.
5 W. L. Warren, D. Dimos, G. E. Pike, K. Vanheusden and R. Ramesh, *Appl. Phys. Lett.*, 1995, **67**, 1689.
6 X. Ren, *Nat. Mater.*, 2004, **3**, 91–94.
7 R. A. Eichel, *Phys. Chem. Chem. Phys.*, 2011, **13**, 368–384.
8 D. M. Smyth, M. P. Harmer and P. Peng, *J. Am. Ceram. Soc.*, 1989, **72**, 2276–2278.
9 J. Chen, H. M. Chan and M. P. Harmer, *J. Am. Ceram. Soc.*, 1989, **72**, 593–598.
10 Y. H. Chen, K. Uchino and D. Viehland, *J. Appl. Phys.*, 2001, **89**, 3928–3933.
11 T. R. Shrout, W. Huebner, C. A. Randall and A. D. Hilton, *Ferroelectrics*, 1989, **93**, 361–372.
12 Y. Wang, Z. Gui, Y. C. Chan, L. Li and X. Zhang, *J. Mater. Sci.: Mater. Electron.*, 1996, **7**, 133–135.
13 U. Plaznik, M. Vrabelj, Z. Kutnjak, B. Malič, A. Poredoš and A. Kitanovski, *Europhys. Lett.*, 2015, **111**, 57009.
14 A. Bradeško, A. Hedl, L. Fulanović, N. Novak and T. Rojac, *APL Mater.*, 2019, **7**, 071111.
15 Y. Bin, Ma, A. Grünebohm, K. C. Meyer, K. Albe and B. X. Xu, *Phys. Rev. B*, 2016, **94**, 1–10.
16 F. Weyland, A. Bradeško, Y.-B. Ma, J. Koruza, B.-X. Xu, K. Albe, T. Rojac and N. Novak, *Energy Technol.*, 2018, **6**, 1519–1525.
17 A. Grünebohm and T. Nishimatsu, *Phys. Rev. B*, 2016, **93**, 1–12.
18 C. Molin, M. Sanlialp, V. V. Shvartsman, D. C. Lupascu, P. Neumeister, A. Schoenecker and S. Gebhardt, *J. Eur. Ceram. Soc.*, 2015, **35**, 2065–2071.
19 U. Plaznik, A. Kitanovski, B. Rožič, B. Malič, H. Uršič, S. Drnovšek, J. Cilenšek, M. Vrabelj, A. Poredoš and Z. Kutnjak, *Appl. Phys. Lett.*, 2015, **106**, 043903.
20 M. Dragomir, M. Otoničar, M. Vrabelj, L. Fulanović, S. Drnovšek, T. Rojac and B. Malič, *J. Eur. Ceram. Soc.*, 2019, **39**, 1837–1845.
21 M. Vrabelj, H. Uršič, Z. Kutnjak, B. Rožič, S. Drnovšek, A. Benčan, V. Bobnar, L. Fulanović and B. Malič, *J. Eur. Ceram. Soc.*, 2016, **36**, 75–80.
22 D. Wilcox, B. Dove, D. McDavid and D. Greer, *Image Tool*, 2002.
23 W. H. Walton, *Nature*, 1948, **162**, 329–330.
24 S. Stoll and A. Schweiger, *J. Magn. Reson.*, 2006, **178**, 42–55.
25 Q. Jiang, W. Cao and L. E. Cross, *J. Am. Ceram. Soc.*, 1994, **77**, 211–215.
26 J. Grigas, A. Brilingas and V. Kalesinskas, *Ferroelectrics*, 1990, **107**, 61–66.
27 J. Banys, S. Lapinskas, S. Rudys, S. Greicius and R. Grigalaitis, *Ferroelectrics*, 2011, **414**, 64–69.
28 Š. Svirskas, D. Jablonskas, S. Rudys, S. Lapinskas, R. Grigalaitis and J. Banys, *Rev. Sci. Instrum.*, 2020, **91**(3), 035106.
29 J. Grigas, *Microwave Dielectric Spectroscopy of Ferroelectrics and Related Materials*, Routledge, London, 2019.
30 Z. Kutnjak, B. Rožič and R. Pirc, *Wiley Encyclopedia of Electrical and Electronics Engineering*, John Wiley & Sons, Inc., Hoboken, NJ, USA, 2015, pp. 1–19.
31 S. K. Misra, *Phys. B*, 1994, **203**, 193–200.

32 D. Kobor, A. Hajjaji, J. E. Garcia, R. Perez, A. Albareda, L. Lebrun and D. Guyomar, *J. Mod. Phys.*, 2010, **01**, 211–216.
33 L. Liu, X. Li, X. Wu, Y. Wang, W. Di, D. Lin, X. Zhao, H. Luo and N. Neumann, *Appl. Phys. Lett.*, 2009, **95**, 1–5.
34 X. Li, X. Zhao, B. Ren, H. Luo, W. Ge, Z. Jiang and S. Zhang, *Scr. Mater.*, 2013, **69**, 377–380.
35 S. Zhang, L. Lebrun, C. A. Randall and T. R. Shrout, *J. Cryst. Growth*, 2004, **267**, 204–212.
36 L. Zhang, E. Erdem, X. Ren and R.-A. Eichel, *Appl. Phys. Lett.*, 2008, **93**, 202901.
37 J. H. Park, J. Park, J. G. Park, B. K. Kim and Y. Kim, *J. Eur. Ceram. Soc.*, 2001, **21**, 1383–1386.
38 Y. Tang, L. Luo, Y. Jia, H. Luo, X. Zhao, H. Xu, D. Lin, J. Sun, X. Meng, J. Zhu and M. Es-Souni, *Appl. Phys. Lett.*, 2006, **89**, 2–5.
39 Y.-H. Chen, S. Hirose, D. Viehland, S. Takahashi and K. Uchino, *Jpn. J. Appl. Phys.*, 2000, **39**, 4843–4852.
40 L. Luo, W. Li, Y. Zhu and J. Wang, *Solid State Commun.*, 2009, **149**, 978–981.
41 J. Dec, S. Miga, W. Kleemann and B. Dkhil, *Ferroelectrics*, 2008, **363**, 141–149.
42 J. Dec, S. Miga and W. Kleemann, *Ferroelectrics*, 2011, **417**, 82–92.
43 B. Dkhil, J. M. Kiat, G. Calvarin, G. Baldinozzi, S. B. Vakhrushev and E. Suard, *Phys. Rev. B: Condens. Matter Mater. Phys.*, 2001, **65**, 1–8.
44 P. M. Gehring, W. Chen, Z.-G. Ye and G. Shirane, *J. Phys.: Condens. Matter*, 2004, **16**, 7113–7121.
45 G. Xu, G. Shirane, J. R. D. Copley and P. M. Gehring, *Phys. Rev. B: Condens. Matter Mater. Phys.*, 2004, **69**, 064112.
46 A. Koreeda, H. Taniguchi, S. Saikan and M. Itoh, *Phys. Rev. Lett.*, 2012, **109**, 197601.
47 R. Blinc, A. Gregorovič, B. Zalar, R. Pirc and S. G. Lushnikov, *Phys. Rev. B: Condens. Matter Mater. Phys.*, 2000, **61**, 253–257.
48 R. Blinc, J. Dolinšek, A. Gregorovič, B. Zalar, C. Filipič, Z. Kutnjak, A. Levstik and R. Pirc, *Phys. Rev. Lett.*, 1999, **83**, 424–427.
49 M. Eremenko, V. Krayzman, A. Bosak, H. Y. Playford, K. W. Chapman, J. C. Woicik, B. Ravel and I. Levin, *Nat. Commun.*, 2019, **10**, 2728.
50 D. Viehland, M. Wuttig and L. E. Cross, *Ferroelectrics*, 1991, **120**, 71–77.
51 R. Pirc and R. Blinc, *Phys. Rev. B: Condens. Matter Mater. Phys.*, 2007, **76**, 020101.
52 W. Pan, E. Furman, G. O. Dayton and L. E. Cross, *J. Mater. Sci. Lett.*, 1986, **5**, 647–649.
53 Z. Ye, *Ferroelectrics*, 1995, **172**, 19–30.
54 L. Jin, Z. He and D. Damjanovic, *Appl. Phys. Lett.*, 2009, **95**, 012905.
55 T. Schenk, E. Yurchuk, S. Mueller, U. Schroeder, S. Starschich, U. Böttger and T. Mikolajick, *Appl. Phys. Rev.*, 2014, **1**, 0–14.
56 E. Sawaguchi, *J. Phys. Soc. Jpn.*, 1953, **8**, 615–629.
57 M. Davis, D. Damjanovic and N. Setter, *Phys. Rev. B: Condens. Matter Mater. Phys.*, 2006, **73**, 1–16.
58 Z. Kutnjak, R. Blinc and Y. Ishibashi, *Phys. Rev. B: Condens. Matter Mater. Phys.*, 2007, **76**, 1–8.
59 F. Chu, N. Setter and A. K. Tagantsev, *J. Appl. Phys.*, 1993, **74**, 5129–5134.
60 F. Chu, I. M. Reaney and N. Setter, *J. Appl. Phys.*, 1995, **77**, 1671–1676.
61 K. Carl and K. H. Härdtl, *Ferroelectrics*, 1977, **17**, 473–486.
62 A. Tkachuk, *AIP Conference Proceedings*, AIP, 2003, vol. 677, pp. 55–64.
63 I. P. Swainson, C. Stock, P. M. Gehring, G. Xu, K. Hirota, Y. Qiu, H. Luo, X. Zhao, J. F. Li and D. Viehland, *Phys. Rev. B: Condens. Matter Mater. Phys.*, 2009, **79**, 1–14.
64 M. J. Krogstad, P. M. Gehring, S. Rosenkranz, R. Osborn, F. Ye, Y. Liu, J. P. C. Ruff, W. Chen, J. M. Wozniak, H. Luo, O. Chmaissem, Z. G. Ye and D. Phelan, *Nat. Mater.*, 2018, **17**, 718–724.
65 Z. Kutnjak, J. Petzelt and R. Blinc, *Nature*, 2006, **441**, 956–959.
66 N. Novak and Z. Kutnjak, *Ferroelectrics*, 2013, **447**, 40–45.
67 F. Weyland, M. Acosta, M. Vögler, Y. Ehara, J. Rödel and N. Novak, *J. Mater. Sci.*, 2018, **53**, 9393–9400.
68 L. Fulanović, A. Bradeško, N. Novak, B. Malič and V. Bobnar, *J. Appl. Phys.*, 2020, **127**, 184102.
69 Z. Kutnjak, B. Vodopivec and R. Blinc, *Phys. Rev. B: Condens. Matter Mater. Phys.*, 2008, **77**, 054102.
70 Z.-G. Ye, Y. Bing, J. Gao, A. A. Bokov, P. Stephens, B. Noheda and G. Shirane, *Phys. Rev. B: Condens. Matter Mater. Phys.*, 2003, **67**, 104104.
71 T. Rojac, M. Kosec, B. Budic, N. Setter and D. Damjanovic, *J. Appl. Phys.*, 2010, **108**, 074104.
72 T. Rojac, S. Drnovsek, A. Bencan, B. Malic and D. Damjanovic, *Phys. Rev. B*, 2016, **93**, 014102.
73 T. Schenk, U. Schroeder, M. Pešić, M. Popovici, Y. V. Pershin and T. Mikolajick, *ACS Appl. Mater. Interfaces*, 2014, **6**, 19744–19751.
74 J. Peräntie, H. N. Tailor, J. Hagberg, H. Jantunen and Z.-G. Ye, *J. Appl. Phys.*, 2013, **114**, 174105.
75 C. Molin, J. Peräntie, F. Le Goupil, F. Weyland, M. Sanlialp, N. Stingelin, N. Novak, D. C. Lupascu and S. Gebhardt, *J. Am. Ceram. Soc.*, 2017, **100**, 2885–2892.
76 B. Rožič, M. Kosec, H. Uršič, J. Holc, B. Malič, Q. M. Zhang, R. Blinc, R. Pirc and Z. Kutnjak, *J. Appl. Phys.*, 2011, **110**, 064118.
77 Z. Jiang, Y. Nahas, S. Prokhorenko, S. Prosandeev, D. Wang, J. Íñiguez and L. Bellaiche, *Phys. Rev. B*, 2018, **97**, 104110.
78 A. Bradeško, L. Fulanović, M. Vrabelj, M. Otoničar, H. Uršič, A. Henriques, C. C. Chung, J. L. Jones, B. Malič, Z. Kutnjak and T. Rojac, *Acta Mater.*, 2019, **169**, 275–283.
79 D. Jablonskas, R. Grigalaitis, J. Banys, A. A. Bokov and Z.-G. Ye, *Appl. Phys. Lett.*, 2015, **107**, 142905.
80 X. Zhao, W. Qu, X. Tan, A. A. Bokov and Z.-G. Ye, *Phys. Rev. B: Condens. Matter Mater. Phys.*, 2009, **79**, 144101.

